

Fuse4Seg: Image Fusion for Multi-Modal Medical Segmentation via Bi-level Optimization

Yuchen Guo¹, Junli Gong², Hongmin Cai³, Yiu-ming Cheung⁴, Weifeng Su⁵

¹Northwestern University ²Northeastern University ³South China University of Technology

⁴Hong Kong Baptist University ⁵Beijing Normal - Hong Kong Baptist University

yuchenguo2027@u.northwestern.edu, wfsu@bnbu.edu.cn

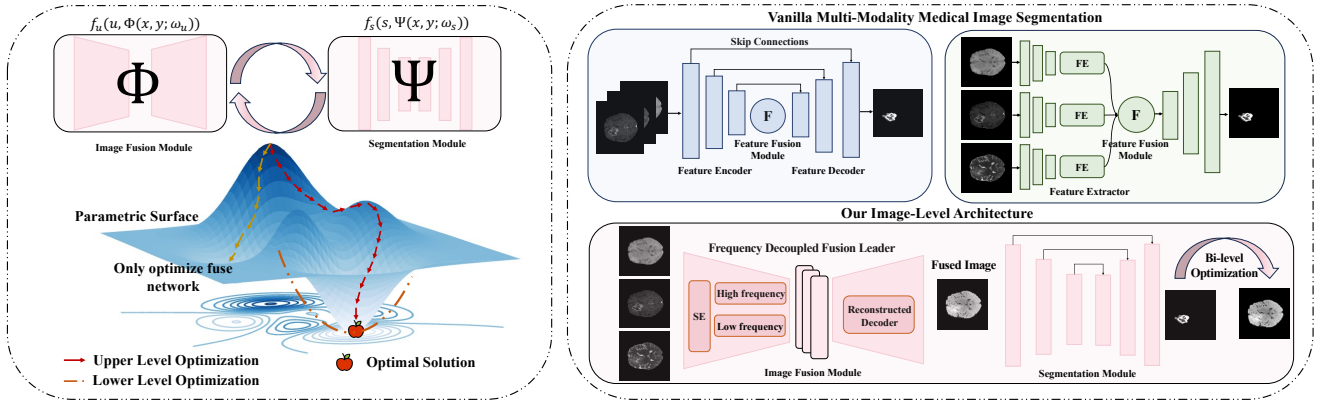


Figure 1. (left) The bi-level optimization learning process with fusion task as the leader and segmentation task as follower. (right) Existing Multi-Modality Medical Image Segmentation Methods vs. Our Fuse4Seg.

Abstract

Multi-modal medical image fusion is traditionally optimized for human visual perception, aiming to maximize generic contrast and structural fidelity. However, when these visually pleasing fused images are deployed in automated clinical workflows, this visual-semantic discrepancy causes task-agnostic feature degradation, inadvertently smoothing out critical, high-frequency tumor boundaries. To bridge this semantic gap, we propose **Fuse4Seg**, a novel framework that reformulates multi-modal fusion as a cooperative bi-level optimization problem with medical segmentation. Rather than relying on rigid visual metrics, our fusion leader dynamically updates its feature extraction strategy driven directly by semantic gradients backpropagated from the downstream segmentation follower. To guarantee robust physical fidelity alongside semantic utility, we design a frequency-decoupled architecture stringently regularized by a Frequency Decomposition Loss and a Spatial Gradient Loss. This explicit physical anchor prevents anatomical distortion and ensures the lossless preservation of task-critical details. Extensive experiments demon-

strate that our task-aware, single-channel fused prior generalizes seamlessly across diverse multi-scale modalities. More impressively, it remarkably surpasses contemporary dual-channel segmentation state-of-the-arts while explicitly providing a readable, "glass-box" physical image to foster clinical visual interpretability and trust.

1. Introduction

Multi-modal Medical Image Fusion (MIF) plays an indispensable role in modern clinical diagnostics [4, 14]. By integrating the complementary physical properties of diverse imaging modalities—such as combining the high spatial resolution of anatomical T1ce MRI with the distinct lesion contrast of FLAIR, or merging MRI with functional PET/SPECT—fusion models generate comprehensive representations that significantly aid human interpretation [26]. Recently, advanced generative architectures, including Diffusion models and state space models (e.g., Mamba), have pushed MIF to unprecedented heights, generating fused images with remarkable visual fidelity and structural similarity [34, 39].

Despite their visual appeal, modern clinical workflows

increasingly rely on automated downstream analysis, such as tumor segmentation, to provide objective, quantitative assessments. Herein lies a critical bottleneck: existing MIF techniques are predominantly ported from natural image domains and are rigorously optimized for *human visual perception* (maximizing generic contrast or global entropy) [16, 28]. They operate completely disjointly from downstream machine vision tasks. Consequently, when these visually pleasing fused images are fed into segmentation networks, critical task-specific high-frequency gradients—such as subtle, highly irregular tumor boundaries—are often inadvertently smoothed out or overshadowed by synthetic textures. This phenomenon is task-agnostic feature degradation, which stems from a fundamental **visual-semantic discrepancy**: *the objective misalignment between low-level visual reconstruction and high-level scene understanding*.

To fundamentally bridge this semantic gap, we present *Fuse4Seg*. Instead of treating fusion and segmentation as isolated pipelines, we formulate their intertwined dependency as a cooperative bi-level optimization problem. In this hierarchy, the image fusion network acts as the upper-level leader, while the segmentation network acts as the lower-level follower. Rather than blindly maximizing generic visual metrics, the fusion leader dynamically updates its parameters driven directly by the semantic gradients backpropagated from the downstream follower. This forces the fusion network to intelligently compress multi-modal information into a single-channel, *task-aware prior* that explicitly maximizes downstream segmentation utility while discarding redundant physical noise.

Our fusion leader employs a frequency-decoupled architecture, utilizing Transformers [29] to model macroscopic tissue contrast and Invertible Neural Networks (INNs) [2] to losslessly preserve sharp pathological margins. These extractors are stringently regularized by a Frequency Decomposition Loss and a Spatial Gradient Loss to ensure the task-driven fusion strictly preserves anatomical structures rather than collapsing into adversarial noise. Crucially, in stark contrast to contemporary multi-channel segmentation pipelines that process raw modalities through uninterpretable “black-box” latent spaces, our framework explicitly bottlenecks the multi-modal information into a readable, single-channel “glass-box” physical image. This paradigm shift not only alleviates the computational burden on the downstream network but also provides crucial visual interpretability, allowing clinicians to transparently verify the biological basis of the automated diagnosis. Based on the above, our main contributions are summarized:

- We propose *Fuse4Seg*, a novel framework that reformulates multi-modal medical image fusion as a cooperative bi-level optimization problem, advancing the paradigm from human-perception-driven visual en-

hancement to task-driven semantic fusion.

- We design a physically-anchored joint architecture. By integrating a Frequency Decomposition Loss and a Spatial Gradient constraint, we prevent adversarial degradation under semantic pressure, perfectly balancing anatomical fidelity (physics) with diagnostic accuracy (semantics).
- Extensive experiments demonstrate that our single-channel prior remarkably surpasses contemporary dual-channel segmentation SOTAs across diverse modalities. Crucially, bottlenecking abstract features into a physical image provides “glass-box” visual interpretability, fostering essential clinical trust.

2. Related Works

2.1. Medical Image Segmentation

Medical image segmentation is pivotal for delineating anatomical and pathological structures [3, 23, 30]. While early advancements were driven by CNN-based U-shaped architectures [8, 12] and later revolutionized by Transformer-based models for global context modeling (e.g., TransUNet [7], Swin-Unet [6], and Mamba-based variants [32]), modern clinical scenarios increasingly rely on *multi-modal* inputs. This dominant paradigm simply employs channel-wise stacking at the input level (e.g., nnUNet [13]). However, this brute-force feature-level fusion heavily inflates computational overhead and operates as a “black-box,” entirely neglecting the interpretable, holistic physical priors that a unified fused image could provide.

2.2. Medical Image Fusion

Existing image fusion methods primarily include autoencoder-based models [10, 37, 40], GANs [17, 21], diffusion models [27, 36, 39], and recent Mamba architectures [34]. Most of these techniques are rigidly optimized for *human visual perception* (maximizing generic structural similarity) [18, 38]. When deployed in automated diagnostic pipelines, this visual-centric objective inherently causes task-agnostic feature degradation. While some recent natural image fusion models have begun incorporating downstream losses heuristically [17, 19], medical domains lack a rigorous mathematical framework to align fusion with complex semantic targets. Our *Fuse4Seg* successfully bridges this critical gap in MIF by formulating the interaction as a cooperative bi-level optimization problem, explicitly generating a task-driven physical prior.

3. Methodology

3.1. Bi-level Optimization Formulation

Medical Image Fusion (MIF) is conventionally treated as an isolated preprocessing step prior to Medical Image Segmentation (MIS). However, optimizing fusion independently often leads to the loss of critical semantic features required by downstream tasks. To bridge this gap, we model the joint fusion and segmentation process as a Stackelberg game, where the fusion module acts as the leader (upper task) and the segmentation module acts as the follower (lower task).

Let $x_1, x_2 \in \mathbb{R}^{H \times W}$ denote the input medical images from two different modalities (e.g., T1ce and FLAIR). We define the fusion network as Φ parameterized by θ_f , which generates the single-channel fused image $x_f = \Phi(x_1, x_2; \theta_f)$. Subsequently, the segmentation network Ψ , parameterized by θ_s , takes x_f as input to predict the semantic mask $\hat{y} = \Psi(x_f; \theta_s)$.

The interdependence between fusion and segmentation can be mathematically formulated as a bi-level optimization problem:

$$\begin{aligned}
 \min_{\theta_f} \quad & \mathcal{L}_{upper}(\theta_f, \theta_s^*) \\
 & = \mathcal{L}_{seg}(\Psi(\Phi(x_1, x_2; \theta_f); \theta_s^*), y) + \lambda \mathcal{L}_{fuse}(\theta_f), \\
 \text{s.t.} \quad & \theta_s^*(\theta_f) = \arg \min_{\theta_s} \mathcal{L}_{lower}(\theta_s, \theta_f) \\
 & = \mathcal{L}_{seg}(\Psi(\Phi(x_1, x_2; \theta_f); \theta_s), y).
 \end{aligned} \tag{1}$$

where \mathcal{L}_{seg} represents the task-driven segmentation loss, and \mathcal{L}_{fuse} is an abstract physical regularity term preserving modality-specific textures and anatomical boundaries. To eliminate ambiguity, in practical implementation, this regularization is instantiated as a combination of decomposition and spatial gradient constraints, defined as $\lambda \mathcal{L}_{fuse}(\theta_f) \triangleq \alpha \mathcal{L}_{decomp} + \beta \mathcal{L}_{grad}$. Unlike previous disjointed methods, Eq. 1 enforces that the optimal fusion parameters θ_f are explicitly driven by the performance of the optimal segmentation network θ_s^* .

where \mathcal{L}_{seg} represents the task-driven segmentation loss, and \mathcal{L}_{fuse} is an abstract physical regularity term preserving modality-specific textures and anatomical boundaries. To eliminate ambiguity, in practical implementation, this regularization is instantiated as a combination of decomposition and spatial gradient constraints, defined as $\lambda \mathcal{L}_{fuse}(\theta_f) \triangleq \alpha \mathcal{L}_{decomp} + \beta \mathcal{L}_{grad}$. Unlike previous disjointed methods, Eq. 1 enforces that the optimal fusion parameters θ_f are explicitly driven by the performance of the optimal segmentation network θ_s^* .

Algorithm 1 Cooperative Training Strategy

Input: Init. fusion params θ_f , seg. params θ_s , EMA $\hat{\theta}_f \leftarrow \theta_f$.

Multi-modal dataset \mathcal{D} , inner steps K , decay m .

Output: Optimized EMA fusion $\hat{\theta}_f$, seg. params θ_s^* .

```

# Stage 1: Follower Warm-up
1: for epoch = 1 to  $E_{warm}$  do
2:   Freeze  $\theta_f$ . Generate prior  $x_{avg} = \frac{1}{2}(x_1 + x_2)$ .
3:   Update  $\theta_s$  using  $\mathcal{L}_{seg}(\Psi(x_{avg}; \theta_s), y)$ .
4: end for

# Stage 2: Asymmetric Bi-level Rollout
5: while not converged do
6:   Sample batch  $\mathcal{B}$ , split into  $\mathcal{D}_{tr}$ ,  $\mathcal{D}_{val}$  (patient-level).
# Inner Loop: Follower Update
7:   Unfreeze  $\theta_s$ . Freeze  $\theta_f$ .
8:   for  $k = 1$  to  $K$  do
9:     Fused images on  $\mathcal{D}_{tr}$ :  $x_f^{(tr)} = \Phi(x_1, x_2; \theta_f)$ .
10:     $\theta_s \leftarrow \theta_s - \eta_s \nabla_{\theta_s} \mathcal{L}_{seg}(\Psi(x_f^{(tr)}; \theta_s), y^{(tr)})$ .
11:   end for
# Outer Loop: Leader Update (Semantic Guided)
12:   Freeze  $\theta_s$ . Unfreeze  $\theta_f$ .
13:   Fused images on  $\mathcal{D}_{val}$ :  $x_f^{(val)} = \Phi(x_1, x_2; \theta_f)$ .
14:   Compute upper loss with physical anchor (Eq. 4):
15:    $\mathcal{L}_{upper} = \mathcal{L}_{seg}|_{\mathcal{D}_{val}} + \alpha \mathcal{L}_{decomp} + \beta \mathcal{L}_{grad} + \gamma \mathcal{L}_{recon}$ .
16:   Update fusion net:  $\theta_f \leftarrow \theta_f - \eta_f \nabla_{\theta_f} \mathcal{L}_{upper}$ .
17:   Update EMA params:  $\hat{\theta}_f \leftarrow m \hat{\theta}_f + (1 - m) \theta_f$ .
18: end while

```

3.2. First-Order Cooperative Training Strategy

Solving the exact bi-level optimization in Eq. 1 is computationally intractable for deep neural networks due to the requirement of calculating the optimal θ_s^* for every fusion update. To efficiently solve this while preventing the framework from collapsing into adversarial noise, we design an advanced, empirically stable first-order alternating strategy. This strategy features a two-stage training paradigm: a Follower Warm-up stage and an Asymmetric Bi-level Rollout stage, regularized by a strict patient-level data-splitting protocol.

Stage 1: Follower Warm-up. Initializing both the fusion leader and segmentation follower from scratch simultaneously inevitably leads to optimization divergence. To establish a stable semantic baseline, we freeze the fusion network and utilize a deterministic physical prior (e.g., the average of the multi-modal inputs, $x_{avg} = \frac{1}{2}(x_1 + x_2)$) to train the segmentation follower for an initial E_{warm} epochs. This guarantees the follower possesses rudimentary tumor-localization capabilities before providing semantic guidance.

Stage 2: Asymmetric Bi-level Rollout. After warm-

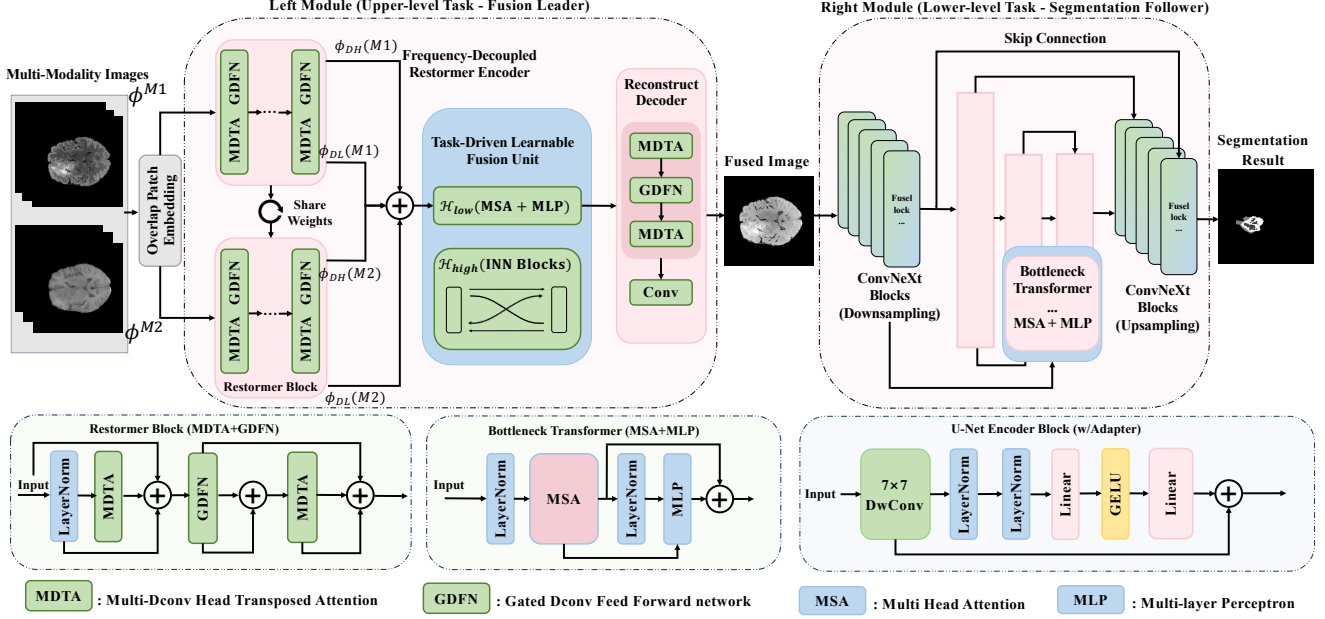


Figure 2. The overall framework of our Fuse4Seg, which consist of a fusion module and a segmentation module.

up, we activate the bi-level cooperative loop. Within each batch \mathcal{B} , we partition the data into two disjoint subsets at the patient-level: \mathcal{D}_{tr} for training the follower and \mathcal{D}_{val} for updating the leader.

Inner Loop (Follower Update): Theoretical bi-level optimization assumes the follower achieves a local optimum θ_s^* given the current leader θ_f . To closely approximate this, we employ an **asymmetric update scheme**. For every fusion update, the segmentation network performs K consecutive gradient descents on \mathcal{D}_{tr} :

$$\begin{aligned} \theta_s^{(k)} \leftarrow & \theta_s^{(k-1)} \\ & - \eta_s \nabla_{\theta_s} \mathcal{L}_{seg} \left(\Psi(\Phi(x_1, x_2; \theta_f); \theta_s^{(k-1)}), y \right) \Big|_{\mathcal{D}_{tr}}, \\ & k \in \{1, \dots, K\}, \end{aligned} \quad (2)$$

Outer Loop (Leader Update): After K inner steps, we freeze θ_s and update the fusion network on \mathcal{D}_{val} . Driven by the semantic gradients backpropagated through the optimized follower, the leader dynamically refines its fusion strategy. To prevent the fusion image from collapsing into task-overfitted adversarial artifacts, we explicitly enforce a lightweight physical anchor via a reconstruction loss (\mathcal{L}_{recon}). The upper-level objective simplifies to:

$$\mathcal{L}_{upper} = \mathcal{L}_{seg} \Big|_{\mathcal{D}_{val}} + \alpha \mathcal{L}_{decomp} + \beta \mathcal{L}_{grad} + \gamma \mathcal{L}_{recon}. \quad (3)$$

The parameter θ_f is then updated via direct partial derivatives. Furthermore, to enhance the physical stability of the generated fusion prior during clinical inference, we maintain an Exponential Moving Average (EMA) of the fusion

network weights:

$$\hat{\theta}_f \leftarrow m \hat{\theta}_f + (1 - m) \theta_f, \quad (4)$$

where m is the momentum decay rate. The complete training procedure is detailed in Algorithm 1.

3.3. Fusion Module

3.3.1 Frequency-Decoupled Encoder

In multi-modal neuroimaging, diagnostic information is intrinsically stratified across spatial frequencies. Low-frequency components typically govern macroscopic anatomical topology and global tissue contrast, and high-frequency signals encapsulate crucial modality-specific pathological signatures, such as sharp enhancing tumor margins, diffuse edema boundaries, and intricate microvascular textures. To explicitly leverage this biological property and prevent the feature entanglement of healthy structural background with subtle lesion details, our encoder first processes the source images through shared Restormer blocks to establish a robust global representation. Subsequently, to avoid task-agnostic feature degradation, the network branches into two specialized frequency-oriented extractors.

For low-frequency features (F_{low}^1, F_{low}^2) representing macroscopic structures and base intensity, we employ standard Multi-Head Self-Attention (MSA) and MLP layers. Conversely, for high-frequency features (F_{high}^1, F_{high}^2) capturing critical diagnostic edges (e.g., subtle tumor boundaries), we strictly prevent information loss by employing

Invertible Neural Network (INN) blocks. Following the architectural design of CDDFuse [37], the INN block utilizes Haar wavelet transformations to squeeze spatial dimensions, followed by affine coupling layers. Specifically, the intermediate feature z is split along the channel dimension into z_1 and z_2 , undergoing sequential transformations:

$$z'_1 = z_1 \odot \exp(\theta_\rho(z_2)) + \theta_\eta(z_2), \quad z'_2 = z_2 + \theta_\phi(z'_1), \quad (5)$$

where \odot denotes element-wise multiplication, and θ_ρ , θ_η , and θ_ϕ represent arbitrary non-linear functions modeled by dense convolutional blocks [37]. The output is then concatenated as $z' = [z'_1, z'_2]$. This rigorously invertible design guarantees zero-loss preservation of high-frequency pathological gradients during the forward pass.

3.3.2 Learnable Fusion Unit

To seamlessly integrate the decoupled features under the guidance of downstream semantic gradients, we discard static arithmetic rules in favor of fully learnable extraction modules (\mathcal{H}_{low} and \mathcal{H}_{high}). The frequency-specific features are first aggregated via element-wise addition and then dynamically optimized:

$$\begin{aligned} F_{low}^{fused} &= \mathcal{H}_{low}(F_{low}^1 + F_{low}^2), \\ F_{high}^{fused} &= \mathcal{H}_{high}(F_{high}^1 + F_{high}^2). \end{aligned} \quad (6)$$

Here, \mathcal{H}_{low} employs MSA and MLP layers to establish optimal global contrast, while \mathcal{H}_{high} utilizes sequential INN blocks to implicitly learn the optimal spatial weighting for high-frequency pathological details. This data-driven aggregation ensures that the feature selection process adapts strictly to the semantic pressure from the segmentation follower. Finally, an anchor-free Transformer decoder reconstructs the single-channel fused image x_f from the concatenated features $\{F_{low}^{fused}, F_{high}^{fused}\}$. To guarantee physical validity and stabilize downstream segmentation, x_f is strictly constrained to $[0, 1]$ domain via Min-Max normalization.

3.4. Segmentation Module

To efficiently decode the task-driven fused prior x_f , our segmentation module employs a Hybrid CNN-Transformer U-shape architecture. The hierarchical backbone utilizes ConvNeXt blocks [33] with large-kernel (7×7) depthwise convolutions, naturally capturing expansive heterogeneous pathologies (e.g., peritumoral edema) with minimal parameter overhead. To preserve fine-grained spatial details, symmetrical skip connections fuse high-resolution features directly into the decoder. Crucially, a Transformer Bottleneck with Multi-Head Self-Attention (MSA) is embedded at the lowest resolution to model long-range global semantic dependencies. This hybrid design optimally balances precise

anatomical boundary localization with comprehensive context understanding, ultimately providing the robust semantic gradients necessary to guide our upstream fusion leader.

3.5. Objective Functions

3.5.1 Lower-Level Objective (Segmentation Follower)

In the inner loop of the bi-level optimization, the segmentation network (parameterized by θ_s) acts as the follower. Its sole objective is to achieve optimal tumor delineation given the current fused prior generated by the leader. The lower-level objective \mathcal{L}_{lower} is formulated using a combination of Cross-Entropy (CE) loss and a weighted multi-class Dice loss. To address the severe class imbalance among the background, necrotic core, peritumoral edema, and enhancing tumor, the Dice loss heavily penalizes misclassifications in the foreground:

$$\mathcal{L}_{Dice} = 1 - \frac{1}{C} \sum_{c=1}^C w_c \frac{2 \sum_i p_{c,i} y_{c,i} + \epsilon}{\sum_i p_{c,i} + \sum_i y_{c,i} + \epsilon},$$

where $p_{c,i}$ and $y_{c,i}$ denote the predicted probability and ground truth for class c at pixel i , ϵ is a smoothing factor, and w_c represents the class-specific penalty weight. The total lower-level objective is defined as:

$$\mathcal{L}_{lower}(\theta_s; \theta_f) = \mathcal{L}_{Dice} + \mathcal{L}_{CE}.$$

During the asymmetric inner steps, θ_s is optimized exclusively by minimizing \mathcal{L}_{lower} on the training split \mathcal{D}_{tr} .

3.5.2 Upper-Level Regularizations

For the outer loop, the fusion network (parameterized by θ_f) acts as the leader. While its primary driving force is the semantic validation loss backpropagated from the optimized follower, updating solely based on this can lead to task-overfitted adversarial artifacts. Therefore, we introduce three complementary physical regularizations:

Frequency Decomposition Loss (\mathcal{L}_{decomp}): To explicitly enforce the separation of modality-shared structure and modality-specific details, we use a Correlation Coefficient (CC)-based penalty:

$$\mathcal{L}_{decomp} = \frac{[CC(F_{high}^1, F_{high}^2)]^2}{1.01 + CC(F_{low}^1, F_{low}^2)}.$$

This objective aggressively minimizes the correlation of high-frequency textures while maximizing the correlation of low-frequency anatomy.

Spatial Gradient Loss (\mathcal{L}_{grad}): To ensure the sharpest diagnostic boundaries from source modalities are retained, we apply a gradient-based penalty using the Sobel operator ∇ :

$$\mathcal{L}_{grad} = \|\nabla x_f - \max(\nabla x_1, \nabla x_2)\|_1.$$

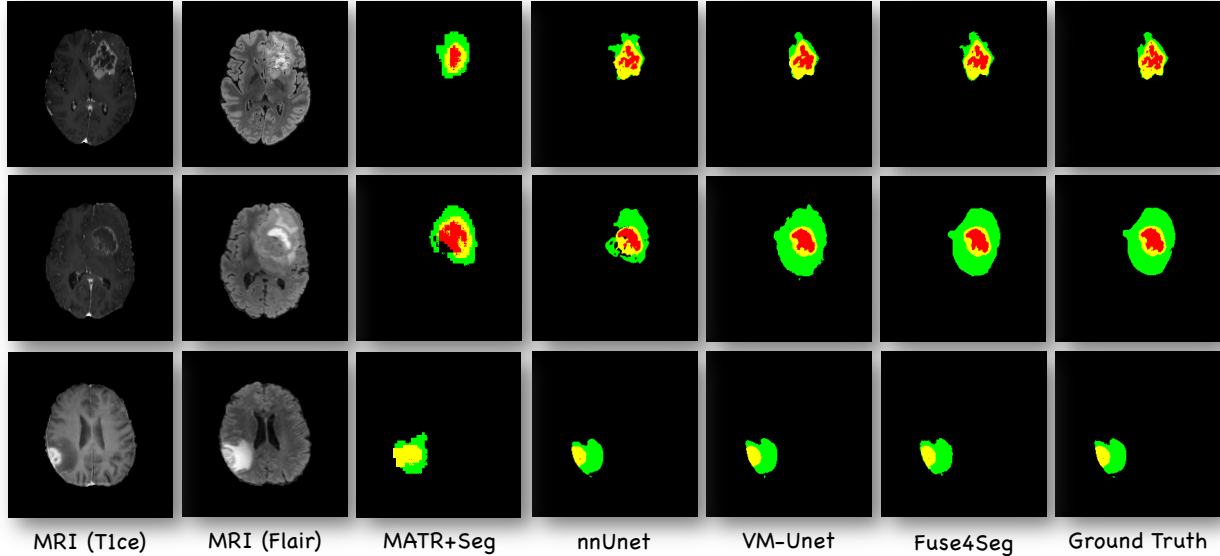


Figure 3. Qualitative comparison with other SOTA medical segmentation methods.

Physical Reconstruction Anchor (\mathcal{L}_{recon}): To guarantee the clinical readability of the fused image and prevent catastrophic physical collapse during the task-driven updates, we introduce a lightweight Mean Squared Error (MSE) anchor:

$$\mathcal{L}_{recon} = \|x_f - \frac{1}{2}(x_1 + x_2)\|_2^2.$$

3.5.3 Total Upper-Level Objective (Fusion Leader)

Ultimately, the fusion leader is optimized on the validation split \mathcal{D}_{val} by minimizing the comprehensive upper-level objective. This formulation elegantly balances the downstream semantic guidance (evaluated on the optimal follower θ_s^*) with the aforementioned physical constraints:

$$\begin{aligned} \mathcal{L}_{upper}(\theta_f) = & \mathcal{L}_{lower}(\theta_s^*) \Big|_{\mathcal{D}_{val}} + \alpha \mathcal{L}_{decomp} \\ & + \beta \mathcal{L}_{grad} + \gamma \mathcal{L}_{recon}, \end{aligned}$$

where α , β , and γ are empirical hyperparameters strictly controlling the trade-off between task-driven performance and physical image fidelity.

4. Experiments

4.1. Experimental Setup

Our framework is implemented in PyTorch and trained on a single NVIDIA A100 GPU. We first conduct a Follower Warm-up stage for 40 epochs, where the segmentation network is solely optimized using a deterministic physical prior (i.e., the average of the multi-modal inputs) to es-

tablish a stable semantic baseline. Subsequently, the asymmetric bi-level rollout stage is executed for 120 epochs. During this stage, to ensure the follower closely approximates the local optimum, the segmentation network performs $K = 5$ inner gradient updates for every single outer update of the fusion leader. Both networks are optimized using the AdamW optimizer with a weight decay of 1×10^{-5} , coupled with a cosine annealing learning rate scheduler. The initial learning rates for the fusion leader and segmentation follower are empirically set to 1×10^{-4} and 3×10^{-4} , respectively. To maintain a batch size of 8, we leverage Automatic Mixed Precision (AMP) training. For the upper-level objective, the optimization trade-off parameters are set as $\alpha = 1.0$, $\beta = 5.0$, and $\gamma = 0.05$ (for the lightweight physical reconstruction anchor). Additionally, the Exponential Moving Average (EMA) momentum decay rate for stabilizing the fusion leader’s weights is set to $m = 0.99$.

4.2. Medical Image Segmentation Results

Dataset. We evaluate our framework on the BraTS 2021 dataset [22], which provides comprehensive multi-modal MRI scans accompanied by expert-annotated ground truths. We strategically select T1-weighted contrast-enhanced (T1ce) and FLAIR as our representative source modalities. Clinically, T1ce strictly highlights the gadolinium-enhancing tumor core (ET) and necrotic regions (NCR), FLAIR exceptionally delineates the peritumoral edema (ED) spreading into healthy brain tissue by suppressing cerebrospinal fluid signals. Fusing these two modalities provides the most critical anatomical and pathological boundaries required for holistic brain tumor analysis.

Table 1. Quantitative segmentation results on the BraTS 2021 dataset utilizing T1ce and FLAIR modalities. All disjoint fusion baselines are evaluated using our identical segmentation backbone. The best results are highlighted in **bold**, and the second-best are underlined.

Method	NCR (Necrotic Core)		ED (Peritumoral Edema)		ET (Enhancing Tumor)		Average	
	Dice ↑	IoU ↑	Dice ↑	IoU ↑	Dice ↑	IoU ↑	Mean Dice ↑	Mean IoU ↑
<i>Disjoint Fusion-Segmentation Pipelines</i>								
DDFM + Seg	0.765	0.665	0.785	0.675	0.800	0.710	0.783	0.683
BSAFusion + Seg	0.775	0.675	0.795	0.685	0.810	0.720	0.793	0.693
MATR + Seg	0.780	0.685	0.805	0.690	0.820	0.730	0.801	0.701
TFS-Diff + Seg	0.785	0.695	0.815	0.700	0.835	0.745	0.811	0.713
CDDFuse + Seg	0.795	0.700	0.825	0.705	0.840	0.750	0.820	0.718
FusionMamba + Seg	0.802	0.710	0.835	0.715	0.850	0.760	0.829	0.728
<i>Direct Multi-Channel Segmentation</i>								
transU-Net	0.820	0.730	0.880	0.745	0.905	0.820	0.868	0.765
nnU-Net	0.810	0.724	0.895	0.750	0.912	0.824	0.872	0.766
CENet (2025)	0.835	0.740	0.899	0.759	0.912	0.832	0.882	0.777
VM-UNet	<u>0.875</u>	<u>0.798</u>	0.912	<u>0.826</u>	<u>0.928</u>	<u>0.870</u>	<u>0.905</u>	<u>0.831</u>
<i>Proposed Method</i>								
Fuse4Seg (Ours)	0.884	0.807	<u>0.908</u>	0.833	0.937	0.884	0.910	0.841

Evaluation Metrics. We rigorously quantify the segmentation performance using the Dice Similarity Coefficient and Intersection over Union (IoU). These metrics are computed across three distinct pathological sub-regions: NCR, ED, and ET, alongside their global averages to evaluate overall delineation accuracy. To ensure a strictly fair comparison, we evaluate our method against two distinct categories of state-of-the-art (SOTA) baselines: (1) **Disjoint Fusion-Segmentation Pipelines:** We construct pipelines using recent SOTA image fusion models, including BSA-Fusion [16], MATR [28], DDFM [39], CDDFuse [37], TFS-Diff [35], and FusionMamba [34]. To eliminate architecture-induced bias, the resulting fused images from all these methods are evaluated using the exact same segmentation backbone and training schedules as ours. (2) **Direct Multi-Channel Methods:** We compare against heavily parameterized multi-channel segmentation models that directly consume all stacked raw modalities, including the nnU-Net [13], TransUNet [7], CENet [5] and VM-UNet [25]. All models are strictly restricted to 2D slice inputs and 2 modalities.

Quantitative Comparison. As shown in Table 1, Fuse4Seg significantly outperforms all disjoint fusion-segmentation pipelines, demonstrating that static visual priors are suboptimal for semantic tasks. More impressively, despite compressing multi-modal inputs into a single-channel prior, our task-driven framework achieves the highest overall Mean Dice, surpassing vanilla segmentation SO-

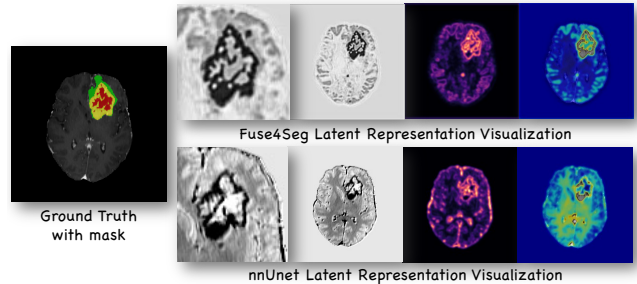


Figure 4. Visual interpretability comparison. Unlike the abstract, uninterpretable latent feature maps of traditional multi-channel networks (e.g., nnUNet), our Fuse4Seg explicitly bottleneck multi-modal information into a highly readable, task-driven fused prior (x_f).

TAs. Excelling in delineating the critical Necrotic Core (NCR), Peritumoral Edema (ED) and Enhancing Tumor (ET), Fuse4Seg’s highly optimized semantic prior establishes a new SOTA for efficient, image fusion-guided segmentation.

Qualitative Comparison. Visual inspections (Fig. 3) further validate the clinical superiority of our framework. As shown, disjoint pipelines (e.g., MATR+Seg) severely smear tumor boundaries, producing blocky artifacts and anatomical hallucinations. Furthermore, while direct multi-channel models (nnU-Net, VM-UNet) capture the general lesion

Table 2. Quantitative comparison of medical image fusion performance. The best results are highlighted in **bold**, and the second-best are underlined. The symbol \uparrow indicates that higher values denote better performance.

Method	Harvard MRI-SPECT							Harvard MRI-PET						
	EN \uparrow	SD \uparrow	MI \uparrow	PSNR \uparrow	SF \uparrow	$Q^{AB/F}$ \uparrow	SSIM \uparrow	EN \uparrow	SD \uparrow	MI \uparrow	PSNR \uparrow	SF \uparrow	$Q^{AB/F}$ \uparrow	SSIM \uparrow
MATR	6.812	43.15	2.754	18.24	14.32	0.612	0.724	6.715	42.10	2.650	17.95	13.85	0.595	0.710
BSAFusion	6.905	44.52	2.915	19.55	15.01	0.638	0.741	6.820	43.65	2.810	19.10	14.65	0.615	0.725
CDDFuse	7.142	46.88	3.210	21.34	16.45	0.685	0.778	7.050	45.90	3.105	20.85	15.95	0.665	0.760
DDFM	7.351	49.21	3.842	20.12	18.22	0.671	0.752	7.250	48.15	3.750	19.85	17.85	0.655	0.740
FusionMamba	7.415	50.14	3.755	<u>22.05</u>	17.54	<u>0.705</u>	<u>0.792</u>	7.310	49.25	3.650	<u>21.55</u>	17.10	<u>0.685</u>	<u>0.775</u>
TFS-Diff	<u>7.450</u>	51.36	4.015	21.88	<u>18.95</u>	0.682	0.765	<u>7.380</u>	50.60	<u>3.818</u>	21.40	<u>18.50</u>	0.660	0.750
Ours (Fuse4Seg)	7.522	<u>50.85</u>	<u>3.912</u>	24.15	19.85	0.742	0.825	7.450	<u>49.85</u>	3.920	23.85	19.25	0.728	0.812

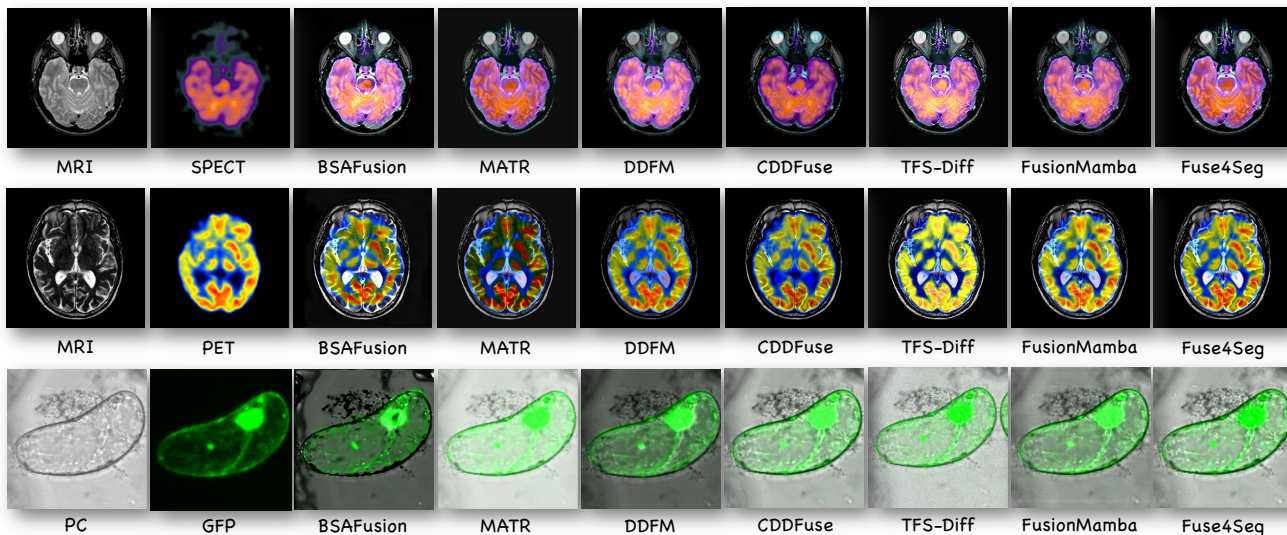


Figure 5. Qualitative comparison with other SOTA methods on Harvard dataset MRI-SPECT, MRI-PET pairs, and GFP database GFP-PC pairs.

area, they frequently over- or under-segment the highly irregular necrotic core (red) and enhancing tumor (yellow). In contrast, Fuse4Seg accurately delineates intricate microvascular boundaries and complex sub-region topologies with a precision that closely mirrors the expert-annotated Ground Truth.

4.3. Visual Interpretability

Vanilla multi-channel models are inherently “black-box,” yielding abstract latent features that lack intuitive physical meaning.

In contrast, Fuse4Seg offers a “glass-box” paradigm by bottlenecking multi-modal inputs into a single-channel physical prior (x_f). As shown in Fig. 4, unlike the uninterpretable activations of standard networks (e.g., nnU-Net), our fused prior explicitly bridges human and machine vision. Driven by downstream semantic gradients, the fusion leader dynamically suppresses redundant background tissue while enhancing contrast in pathological regions. Crucially, strictly regularized by \mathcal{L}_{grad} and \mathcal{L}_{recon} , this enhance-

ment avoids adversarial noise, preserving sharp, anatomically faithful boundaries. This explicit interpretability allows clinicians to effectively “see what the network sees,” verifying that predictions stem from valid biological structures rather than artifactual correlations, thereby fostering essential trust in the diagnostic pipeline.

4.4. Medical Image Fusion Results

Datasets. To rigorously validate the generalization capability of our fusion module beyond the BraTS segmentation task, we extend our evaluation to two fusion benchmarks: the Harvard dataset [15] and the GFP database [1]. From the Harvard dataset, we use MRI-SPECT and MRI-PET modality pairs to assess the framework’s ability to seamlessly integrate high-resolution macroscopic anatomical structures (MRI) with functional metabolic signals (PET/SPECT). Furthermore, to evaluate robustness across drastically different physical scales, we employ Green Fluorescent Protein and Phase Contrast (GFP-PC) image pairs from the GFP database. Training and evaluating of our fu-

Table 3. Ablation study on the core components of our Fuse4Seg framework. Performance is evaluated comprehensively across all tumor sub-regions (NCR, ED, ET) using Dice and IoU metrics.

Model Variants	Components			NCR		ED		ET		Average	
	Bi-level	\mathcal{L}_{decomp}	\mathcal{L}_{grad}	Dice \uparrow	IoU \uparrow	Dice \uparrow	IoU \uparrow	Dice \uparrow	IoU \uparrow	Mean Dice \uparrow	Mean IoU \uparrow
Baseline (Disjoint)	×	×	×	0.795	0.690	0.815	0.715	0.850	0.749	0.820	0.718
Variant A	✓	×	×	0.840	0.745	0.855	0.755	0.900	0.780	0.865	0.760
Variant B	✓	✓	×	0.865	0.775	0.880	0.785	0.919	0.825	0.888	0.795
Ours (Full)	✓	✓	✓	0.884	0.807	0.908	0.833	0.937	0.884	0.910	0.841

sion module on these diverse modalities demonstrates that our frequency-decoupled architecture serves as a highly adaptable, generalized prior generator for both macroscopic and microscopic medical image fusion.

Evaluation Metrics. We benchmark our *Fuse4Seg* against seven state-of-the-art (SOTA) medical image fusion methods, spanning CNN-based, Transformer-based, Diffusion-based, and Mamba-based architectures. The comparative baselines include MATR [28], BSAFusion [16], CDDFuse [37], DDFM [39], TFS-Diff [35] and FusionMamba [34]. To comprehensively evaluate the fusion quality, we select seven widely-adopted objective metrics: Entropy (EN) [24], Standard Deviation (SD) [9], Mutual Information (MI) [20], Peak Signal-to-Noise Ratio (PSNR) [11], Spatial Frequency (SF) [20], Edge Preservation ($Q^{AB/F}$) [20], and Structural Similarity (SSIM) [31].

Quantitative Comparison. As Table 2 reports, explicitly guided by \mathcal{L}_{grad} , Fuse4Seg comprehensively dominates structural and fidelity metrics (PSNR, SF, $Q^{AB/F}$, SSIM), proving it preserves sharp anatomical edges without structural distortion. While generative pipelines like TFS-Diff marginally lead in global statistics (EN, SD), this is anatomically expected; diffusion models often inject synthetic noise that artificially inflates entropy. In contrast, Fuse4Seg tightly bounds the feature space to retain authentic clinical readability, yielding highly robust fused priors across MRI-SPECT and MRI-PET.

Qualitative Comparison. Visual inspections (Fig. 5) corroborate our quantitative superiority across multi-scale modalities. As observed, baseline methods frequently struggle to balance structural and functional information. For instance, MATR and BSAFusion introduce severe color distortions and contrast degradation, while approaches like TFS-Diff tend to over-saturate functional signals, inadvertently masking underlying anatomical boundaries. In contrast, tightly constrained by our spatial gradient loss and physical reconstruction anchor, Fuse4Seg seamlessly integrates the high-frequency structural details of MRI and PC images with the vibrant functional representations of PET,

SPECT, and GFP modalities. Consequently, our method produces sharp, artifact-free fused images with maximal clinical interpretability.

4.5. Ablation Study

To validate the efficacy of our proposed components, we conduct a comprehensive ablation study, incrementally adding the Cooperative Bi-level Optimization (Bi-level), Frequency Decomposition Loss (\mathcal{L}_{decomp}), and Spatial Gradient Loss (\mathcal{L}_{grad}) to a disjoint AutoEncoder baseline.

Effect of Bi-level Optimization. Introducing the alternating bi-level loop significantly boosts overall segmentation performance, particularly for the Enhancing Tumor (ET). This confirms that allowing semantic gradients from the downstream follower to directly backpropagate successfully forces the fusion leader to highlight critical semantic regions, generating a task-aware prior rather than a naive physical blend.

Effect of Frequency Decomposition (\mathcal{L}_{decomp}). To counter potential feature entanglement, we incorporate \mathcal{L}_{decomp} . Enforcing a strict separation between modality-shared anatomical structures and modality-specific high-frequency textures filters out redundant physical noise. This provides a significantly cleaner semantic prior, which is particularly vital for elevating the segmentation accuracy of the intricate Necrotic Core (NCR).

Effect of Spatial Gradient Loss (\mathcal{L}_{grad}). While previous variants capture broad semantics, they lack explicit physical boundary constraints, occasionally over-smoothing local textures. Adding \mathcal{L}_{grad} explicitly forces the fused image to inherit sharp diagnostic boundaries from the source modalities. This physical regularity synergistically maximizes our segmentation performance, proving crucial for delineating the diffuse, highly irregular boundaries of the Peritumoral Edema (ED) and culminating in our state-of-the-art results.

5. Conclusion

In this paper, we propose *Fuse4Seg*, reformulating multi-modal fusion as a cooperative bi-level optimization problem to bridge the gap with high-level semantic segmentation. By abandoning disjoint, human-perception-driven pipelines, our method dynamically compresses diverse modalities into a highly optimized, task-aware single-channel prior. Extensive experiments demonstrate that *Fuse4Seg* achieves state-of-the-art fusion fidelity while remarkably surpassing contemporary dual-channel segmentation SOTAs. Ultimately, by bottlenecking abstract features into a readable “glass-box” physical image, our framework provides crucial visual interpretability, establishing a robust, transparent baseline for task-driven medical diagnosis.

Acknowledgments

This work was supported in part by the Guangdong Provincial Key Laboratory of IRADS (2022B1212010006), in part by the Guangdong Higher Education Upgrading Plan (2021–2025), in part by the Guangdong and Hong Kong Universities “1+1+1” Joint Research Collaboration Scheme, in part by the National Key Research and Development Program of China (2022ZD0117700), in part by the National Natural Science Foundation of China (62325204), and in part by the MSAI program of Northwestern University. The authors would like to thank Zhenghao Wu’s insightful discussions and feedback on the manuscript.

References

- [1] Gfp image dataset. <https://data.jic.ac.uk/Gfp/>. 8
- [2] Lynton Ardizzone, Jakob Kruse, Sebastian Wirkert, Daniel Rahner, Eric W Pellegrini, Ralf S Klessen, Lena Maier-Hein, Carsten Rother, and Ullrich Köthe. Analyzing inverse problems with invertible neural networks. *arXiv preprint arXiv:1808.04730*, 2018. 2
- [3] Reza Azad, Ehsan Khodapanah Aghdam, Amelie Rauland, Yiwei Jia, Atlas Haddadi Avval, Afshin Bozorgpour, Sanaz Karimijafarbigloo, Joseph Paul Cohen, Ehsan Adeli, and Dorit Merhof. Medical image segmentation review: The success of u-net. *IEEE Transactions on Pattern Analysis and Machine Intelligence*, 46(12):10076–10095, 2024. 2
- [4] Muhammad Adeel Azam, Khan Bahadar Khan, Sana Salahuddin, Eid Rehman, Sajid Ali Khan, Muhammad Attique Khan, Seifedine Kadry, and Amir H Gandomi. A review on multimodal medical image fusion: Compendious analysis of medical modalities, multimodal databases, fusion techniques and quality metrics. *Computers in biology and medicine*, 144:105253, 2022. 1
- [5] Afshin Bozorgpour, Sina Ghorbani Kolahi, Reza Azad, Ilker Hacıhaliloglu, and Dorit Merhof. Cenet: Context enhancement network for medical image segmentation. In *International Conference on Medical Image Computing and Computer-Assisted Intervention*, pages 120–129. Springer, 2025. 7
- [6] Hu Cao, Yueyue Wang, Joy Chen, Dongsheng Jiang, Xiaopeng Zhang, Qi Tian, and Manning Wang. Swin-unet: Unet-like pure transformer for medical image segmentation. In *European conference on computer vision*, pages 205–218. Springer, 2022. 2
- [7] Jieneng Chen, Yongyi Lu, Qihang Yu, Xiangde Luo, Ehsan Adeli, Yan Wang, Le Lu, Alan L Yuille, and Yuyin Zhou. Transunet: Transformers make strong encoders for medical image segmentation. *arXiv preprint arXiv:2102.04306*, 2021. 2, 7
- [8] Liang-Chieh Chen, George Papandreou, Iasonas Kokkinos, Kevin Murphy, and Alan L Yuille. Deeplab: Semantic image segmentation with deep convolutional nets, atrous convolution, and fully connected crfs. *IEEE transactions on pattern analysis and machine intelligence*, 40(4):834–848, 2017. 2
- [9] Ahmet M Eskicioglu and Paul S Fisher. Image quality measures and their performance. *IEEE Transactions on communications*, 43(12):2959–2965, 2002. 9
- [10] Yuchen Guo, Ruoxiang Xu, Rongcheng Li, and Weifeng Su. Dae-fuse: An adaptive discriminative autoencoder for multi-modality image fusion. In *2025 IEEE International Conference on Multimedia and Expo (ICME)*, pages 1–6. IEEE, 2025. 2
- [11] Alain Hore and Djemel Ziou. Image quality metrics: Psnr vs. ssim. In *2010 20th international conference on pattern recognition*, pages 2366–2369. IEEE, 2010. 9
- [12] Huimin Huang, Lanfen Lin, Ruofeng Tong, Hongjie Hu, Qiaowei Zhang, Yutaro Iwamoto, Xianhua Han, Yen-Wei Chen, and Jian Wu. Unet 3+: A full-scale connected unet for medical image segmentation. In *ICASSP 2020-2020 IEEE international conference on acoustics, speech and signal processing (ICASSP)*, pages 1055–1059. Ieee, 2020. 2
- [13] Fabian Isensee, Paul F Jaeger, Simon AA Kohl, Jens Petersen, and Klaus H Maier-Hein. nnu-net: a self-configuring method for deep learning-based biomedical image segmentation. *Nature methods*, 18(2):203–211, 2021. 2, 7
- [14] Alex Pappachen James and Belur V Dasarathy. Medical image fusion: A survey of the state of the art. *Information fusion*, 19:4–19, 2014. 1
- [15] B. A. Johnson and J. A. Becker. <http://www.med.harvard.edu/AANLIB/home.html>. 8
- [16] Huafeng Li, Dayong Su, Qing Cai, and Yafei Zhang. Bsa-fusion: A bidirectional stepwise feature alignment network for unaligned medical image fusion. In *Proceedings of the AAAI conference on artificial intelligence*, volume 39, pages 4725–4733, 2025. 2, 7, 9
- [17] Jinyuan Liu, Xin Fan, Zhanbo Huang, Guanyao Wu, Risheng Liu, Wei Zhong, and Zhongxuan Luo. Target-aware dual adversarial learning and a multi-scenario multi-modality benchmark to fuse infrared and visible for object detection. In *Proceedings of the IEEE/CVF conference on computer vision and pattern recognition*, pages 5802–5811, 2022. 2
- [18] Jinyuan Liu, Xin Fan, Ji Jiang, Risheng Liu, and Zhongxuan Luo. Learning a deep multi-scale feature ensemble and an edge-attention guidance for image fusion. *IEEE*

- Transactions on Circuits and Systems for Video Technology*, 32(1):105–119, 2021. 2
- [19] Jinyuan Liu, Zhu Liu, Guanyao Wu, Long Ma, Risheng Liu, Wei Zhong, Zhongxuan Luo, and Xin Fan. Multi-interactive feature learning and a full-time multi-modality benchmark for image fusion and segmentation. In *Proceedings of the IEEE/CVF international conference on computer vision*, pages 8115–8124, 2023. 2
- [20] Jiayi Ma, Yong Ma, and Chang Li. Infrared and visible image fusion methods and applications: A survey. *Information fusion*, 45:153–178, 2019. 9
- [21] Jiayi Ma, Han Xu, Junjun Jiang, Xiaoguang Mei, and Xiaoping Zhang. Ddcgan: A dual-discriminator conditional generative adversarial network for multi-resolution image fusion. *IEEE Transactions on Image Processing*, 29:4980–4995, 2020. 2
- [22] Bjoern H Menze, Andras Jakab, Stefan Bauer, Jayashree Kalpathy-Cramer, Keyvan Farahani, Justin Kirby, Yuliya Burren, Nicole Porz, Johannes Slotboom, Roland Wiest, et al. The multimodal brain tumor image segmentation benchmark (brats). *IEEE transactions on medical imaging*, 34(10):1993–2024, 2014. 6
- [23] Dominik Müller, Iñaki Soto-Rey, and Frank Kramer. Towards a guideline for evaluation metrics in medical image segmentation. *BMC research notes*, 15(1):210, 2022. 2
- [24] J Wesley Roberts, Jan A Van Aardt, and Fethi Babikker Ahmed. Assessment of image fusion procedures using entropy, image quality, and multispectral classification. *Journal of Applied Remote Sensing*, 2(1):023522, 2008. 9
- [25] Jiacheng Ruan, Jincheng Li, and Suncheng Xiang. Vm-unet: Vision mamba unet for medical image segmentation. *ACM Transactions on Multimedia Computing, Communications and Applications*, 2024. 7
- [26] Wei Tan, Prayag Tiwari, Hari Mohan Pandey, Catarina Moreira, and Amit Kumar Jaiswal. Multimodal medical image fusion algorithm in the era of big data. *Neural computing and applications*, 37(28):22995–23015, 2025. 1
- [27] Linfeng Tang, Chunyu Li, and Jiayi Ma. Mask-difuser: A masked diffusion model for unified unsupervised image fusion. *IEEE Transactions on Pattern Analysis and Machine Intelligence*, 2025. 2
- [28] Wei Tang, Fazhi He, Yu Liu, and Yansong Duan. Matr: Multimodal medical image fusion via multiscale adaptive transformer. *IEEE Transactions on Image Processing*, 31:5134–5149, 2022. 2, 7, 9
- [29] Ashish Vaswani, Noam Shazeer, Niki Parmar, Jakob Uszkoreit, Llion Jones, Aidan N Gomez, Łukasz Kaiser, and Illia Polosukhin. Attention is all you need. *Advances in neural information processing systems*, 30, 2017. 2
- [30] Risheng Wang, Tao Lei, Ruixia Cui, Bingtao Zhang, Hongying Meng, and Asoke K Nandi. Medical image segmentation using deep learning: A survey. *IET image processing*, 16(5):1243–1267, 2022. 2
- [31] Zhou Wang, Alan C Bovik, Hamid R Sheikh, and Eero P Simoncelli. Image quality assessment: from error visibility to structural similarity. *IEEE transactions on image processing*, 13(4):600–612, 2004. 9
- [32] Ziyang Wang, Jian-Qing Zheng, Yichi Zhang, Ge Cui, and Lei Li. Mamba-unet: Unet-like pure visual mamba for medical image segmentation. *arXiv preprint arXiv:2402.05079*, 2024. 2
- [33] Sanghyun Woo, Shoubhik Debnath, Ronghang Hu, Xinlei Chen, Zhuang Liu, In So Kweon, and Saining Xie. Convnext v2: Co-designing and scaling convnets with masked autoencoders. In *Proceedings of the IEEE/CVF conference on computer vision and pattern recognition*, pages 16133–16142, 2023. 5
- [34] Xinyu Xie, Yawen Cui, Tao Tan, Xubin Zheng, and Zitong Yu. Fusionmamba: Dynamic feature enhancement for multimodal image fusion with mamba. *Visual Intelligence*, 2(1):37, 2024. 1, 2, 7, 9
- [35] Yushen Xu, Xiaosong Li, Yuchan Jie, and Haishu Tan. Simultaneous tri-modal medical image fusion and super-resolution using conditional diffusion model. In *International conference on medical image computing and computer-assisted intervention*, pages 635–645. Springer, 2024. 7, 9
- [36] Xunpeng Yi, Linfeng Tang, Hao Zhang, Han Xu, and Jiayi Ma. Diff-if: Multi-modality image fusion via diffusion model with fusion knowledge prior. *Information Fusion*, 110:102450, 2024. 2
- [37] Zixiang Zhao, Haowen Bai, Jianshe Zhang, Yulun Zhang, Shuang Xu, Zudi Lin, Radu Timofte, and Luc Van Gool. Cddfuse: Correlation-driven dual-branch feature decomposition for multi-modality image fusion. In *Proceedings of the IEEE/CVF conference on computer vision and pattern recognition*, pages 5906–5916, 2023. 2, 5, 7, 9
- [38] Zixiang Zhao, Haowen Bai, Jianshe Zhang, Yulun Zhang, Kai Zhang, Shuang Xu, Dongdong Chen, Radu Timofte, and Luc Van Gool. Equivariant multi-modality image fusion. In *Proceedings of the IEEE/CVF conference on computer vision and pattern recognition*, pages 25912–25921, 2024. 2
- [39] Zixiang Zhao, Haowen Bai, Yuanzhi Zhu, Jianshe Zhang, Shuang Xu, Yulun Zhang, Kai Zhang, Deyu Meng, Radu Timofte, and Luc Van Gool. Ddfm: Denoising diffusion model for multi-modality image fusion. In *Proceedings of the IEEE/CVF international conference on computer vision*, pages 8082–8093, 2023. 1, 2, 7, 9
- [40] Zixiang Zhao, Shuang Xu, Chunxia Zhang, Junmin Liu, Pengfei Li, and Jianshe Zhang. Didfuse: Deep image decomposition for infrared and visible image fusion. *arXiv preprint arXiv:2003.09210*, 2020. 2